Intermetallics 89 (2017) 1–9

Contents lists available at ScienceDirect

Intermetallics

journal homepage: www.elsevier.com/locate/intermet

The effect of employed loading mode on the mechanical cyclic stabilization of NiTi shape memory alloys

S. Dilibal[a,b,*], R.F. Hamilton[c], A. Lanba[c]

[a] Department of Mechatronics Engineering, Istanbul Gedik University, Istanbul, 34876, Turkey
[b] Department of Mechanical Engineering, The University of Akron, Akron, OH, 44325-3905, USA
[c] Department of Engineering Science and Mechanics, The Pennsylvania State University, 212 Earth-Engineering Sciences Building, University Park, PA, 16802-6812, USA

ARTICLE INFO

Keywords:
Nickel-titanium
Mechanical cycling
Pseudoelastic response
Uniaxial tensile test

ABSTRACT

One of the effective parameters on the characteristic response of the nickel-titanium (NiTi) shape memory alloy (SMA) is the employed loading mode during the uniaxial cycling. In this study, the uniaxial tensile tests are conducted under an extended number of mechanical cycles in order to investigate the effect of force control on the pseudoelastic response of the NiTi SMA. The results which are obtained under the force control are compared with the mixed (force/displacement) control counterpart. An evolutionary stress-strain pattern is observed during the 100 cycles of mechanical loading. Additionally, it is noticed that the residual strain and mechanical hysteresis area also show an evolutionary pattern. The observed evolutionary patterns are delineated in three regimes: (i) early evolution; (ii) approach to a nearly stable stage (transient); and (iii) stabilization stage. Furthermore, the in-situ digital image correlation (DIC) is applied to receive the meso-/micro-scale full-field strain measurements. Severe strain localization is observed under force-controlled tensile test during meso-,/micro-scale DIC analysis.

1. Introduction

Many practical applications of austenitic NiTi shape memory alloys (SMAs) require an extended number of isothermal pseudoelastic cycles [1–3]. The cyclic behavior of the pseudoelastic NiTi SMA needs to be stabilized before using in any industrial, biomedical or aerospace applications. The mechanical cycling (mechanical training) of the NiTi SMA [4–9] is the most common approach to achieve a stabilized pseudoelastic response. The cyclic stabilization depends on many different material or experimental based parameters. A number of previous studies have considered the effect of thermo-mechanical processing (hot/cold working [10] and heat treatment [11,12]), crystallographic orientation [13], Ni concentration [14] on the cyclic deformation of the austenitic NiTi SMA. Other studies have examined the influence of the experimental based parameters; such as testing temperature [15], strain rates [16,17], loading frequency [18], and mean strain [19]. However, the effect of the selected load/unload control mode on the cyclic deformation has not been systematically examined in the SMA literature. The understanding on the link between the employed control mode and the resulting mechanical cyclic stabilization is still limited. Thus, it is necessary to determine how the employed control protocol attributes of the observed cyclic stabilization. The uniaxial experiments are typically conducted under pure force [4,9], pure displacement [15] or mixed [10–14] control. Many uniaxial experiments reported in the SMA literature are conducted in the mixed-control mode. Thus, one of the control modes which is chosen in this study is the mixed-control mode.

This experimental study is dedicated to explore the dependence of the mechanical cyclic stabilization on the employed loading protocol using macro-/meso-/micro-scale investigations. The macroscopic results and the detailed DIC analysis have provided further insight into the stabilization stages.

2. Materials and methods

Hot rolled polycrystalline NiTi bar with a diameter of 32.26 mm was supplied by SAES Smart Materials with a nominal $Ni_{50.8}Ti_{49.2}$ (at.%) composition. Dog-bone tensile test specimens were micro-machined along the rolling direction using electrical discharge machining (EDM) with a final geometry of 10 mm gage length and 3 × 1 mm square cross section, as shown in Fig. 1. This geometry has been obtained from ASTM STP 1329 Symposium on “Small specimen test techniques” [20]. Differential scanning calorimetry (DSC) analysis was conducted between temperature limits of −100 °C and +200 °C with a heating/

* Corresponding author. Department of Mechatronics Engineering, Istanbul Gedik University, Istanbul, 34876, Turkey.
E-mail address: savas.dilibal@gedik.edu.tr (S. Dilibal).

http://dx.doi.org/10.1016/j.intermet.2017.05.014
Received 31 March 2017; Received in revised form 10 May 2017; Accepted 17 May 2017

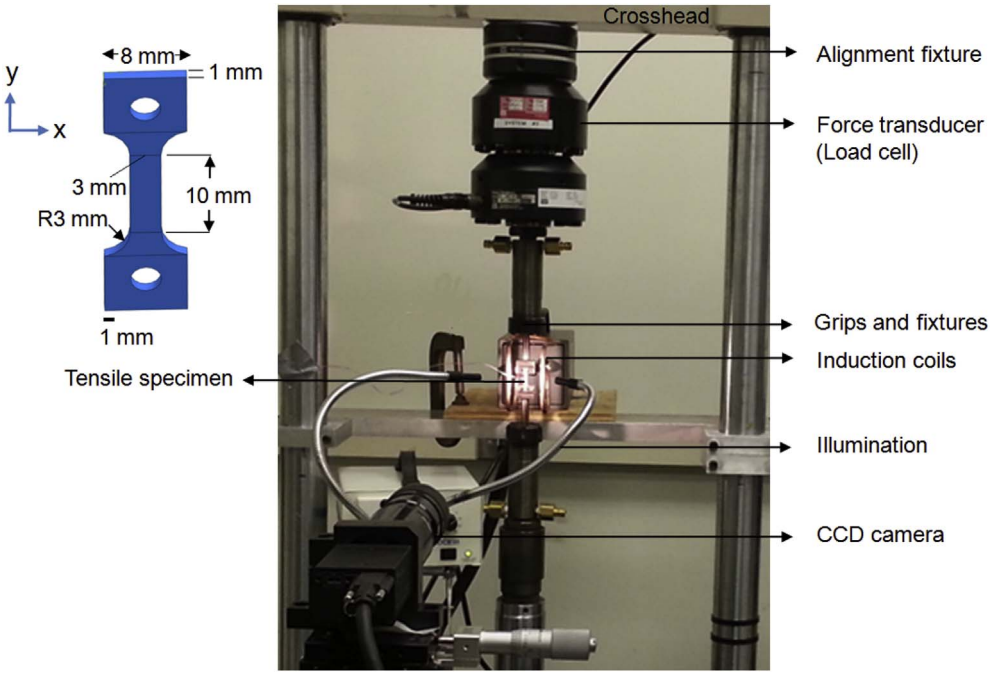

Fig. 1. Experimental setup for the uniaxial cyclic deformation and associated dog-bone specimen geometry.

cooling rate of 10 °C/min, and transformation temperatures were as follows; $A_f = -5$ °C; $A_s = -35$ °C; $M_s = -41$ °C; and $M_f = -55$ °C.

Uniaxial cyclic deformation is studied using two different loading protocols; each in two segments (load-S1 and unload-S2). The first test was conducted under force control for the load segment (S1) as well as unloading segment (S2). The second was carried out under mixed control. In a general *mixed* control mode, the experimental protocol may involve two steps for each cycle: a loading segment (S1) which proceeds under a selected control mode and an unloading segment (S2) which utilizes a different control mode. The current work employs S1-displacement control and S2-force control.

Tensile samples were subjected to an equal number of cycles (100 cycles) in the austenitic state at 35 °C, above the A_f temperature to obtain a pseudoelastic response. Experiments were performed on an MTS 810 servohydraulic testing machine. The experimental setup can be seen in Fig. 1. Uniaxial cyclic deformation was studied using two different loading protocols, each in two segments (load-S1 and unload-S2). The first test was conducted under force control for the load segment (S1) as well as unloading segment (S2). In this force-controlled loading protocol, S1 and S2 correspond to a change in force between a minimum and a maximum force values at a specified rate. The second test was carried out under mixed control with S1-displacement control and S2-force control. In a general *mixed* control mode, the experimental protocol involves two steps for each cycle: a loading segment (S1) which proceeds under a selected control mode and an unloading segment (S2) which utilizes a different control mode. The details of the employed mixed loading control mode and its associated time history is illustrated in Fig. 2.

Cyclic, force-controlled, uniaxial tension tests were performed under a sinusoidal profile by applying a maximum force (1648.5 N) in the loading segment (S1) and returning to a minimum force (0 N) in the unloading segment (S2) under the sinusoidal profile for 100 cycles. An average force rate of 54.95 N $s^{-1}$was specified during the entire cyclic period. The initial and final rates are approaching zero N s^{-1}. In the uniaxial mixed-controlled cyclic test, the following loading protocol was applied under a sinusoidal profile: the loading segment (S1) was performed in displacement-control mode to a maximum displacement value of 0.45 mm with a displacement rate of 0.015 mm s^{-1}. In the unloading segment (S2), the control mode was switched to force-control to a force value of 0 N at force (average) rate of -53.6 N s^{-1}. In the results, we report on the engineering stress which is found by dividing the force over the cross-sectional area of the gage section prior to testing.

An in-situ digital image correlation (DIC) technique was used to investigate the evolution of the local strain variation during cyclic deformation. A general background on DIC and further details on its applications can be found in Ref. [21]. DIC has been used on single and polycrystalline NiTi to obtain the full-field strain data [22,23] and to observe shear dominant loading [24]. The DIC technique measures displacement fields by tracking features on the specimen surface with a random speckle pattern. To perform DIC, a uniform white background was painted on the specimen surface and micron size black speckles were painted on the background using an airbrush. Upon tensile loading, images of the specimen surface were captured with a CCD camera (1600 × 1200pixels) equipped with a zoom lens at a 0.24× magnification. Images and data were captured using Vic-Snap software from Correlated Solutions. Commercially available software (Vic2D) from Correlated Solutions was used to perform the image correlation and the local strain calculations.

Throughout the cyclic loading, one image was captured every 0.5 s. We use an area of interest (AOI) with dimensions (2.3 mm × 13.0 mm) as shown in the schematics in Fig. 3(a). Based on the step size and strain gage filter size, the gage length inherent for DIC analysis is 540 μm and corresponds to meso-scale measurements. Different DIC virtual extensometers (digital extensometers) span different gage lengths and provide meso-scale average strain measurements, as shown in Fig. 3(a). The gage length of extensometer A is equivalent to the specimen gage length (10 mm). A second, B, and third, C, extensometer gage length is 3 mm. The digital extensometers are akin to strain gages or extensometers that are mounted on the specimen. To further scrutinize local strain evolution, within the AOI, average strains are calculated over three differently size regions, as shown in Fig. 3(b): (A) nearly the size of the AOI, 2 mm × 10 mm; (B) within local strain bands, 2 mm × 1 mm, and (C) outside the localized strain bands. The average strains in the regions allow us to find the change in the longitudinal (along the loading direction), transverse and shear strains, which are referred to as e_{yy}, e_{xx}, and e_{xy} respectively.

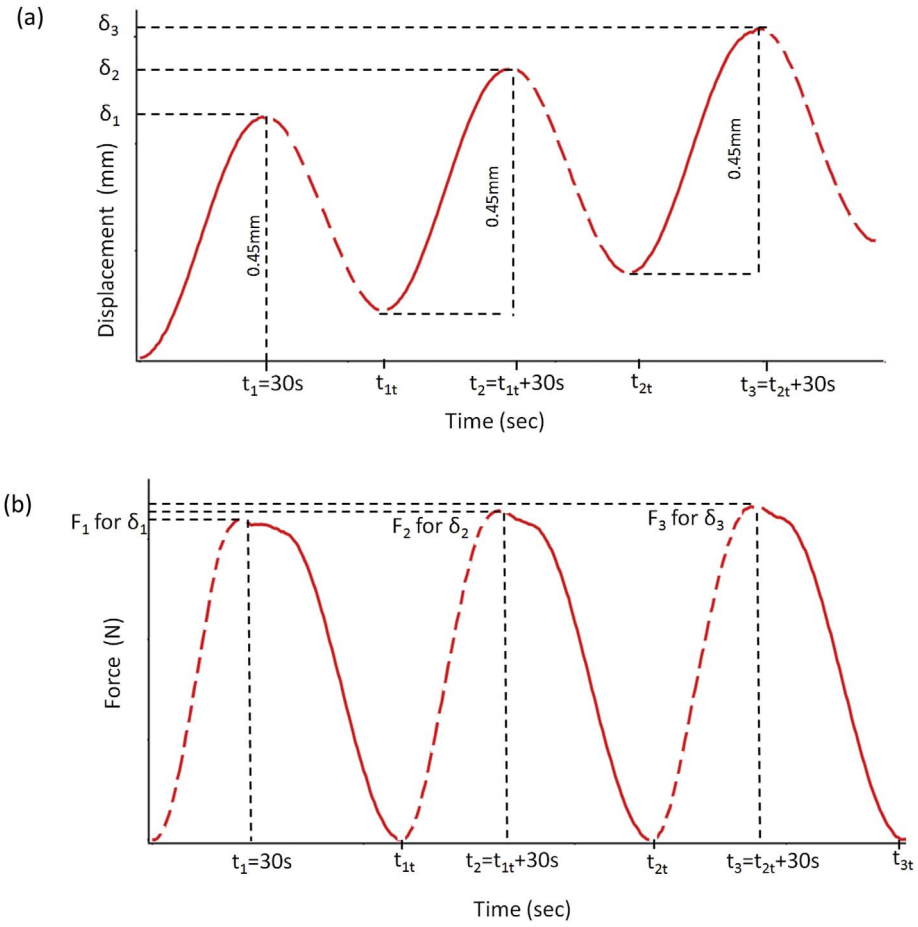

Fig. 2. Mixed controlled (S1-displacement control, S2-force control) cyclic loading and its associated time histories: a) The employed control mode during loading segment (S1), and b) The employed control mode during unloading segment (S1). In the schematic, $\delta_{1,2,3}$ indicates the magnitude of the displacement during each cycle, $t_{1,2,3}$ indicates the end of each loading segment (S1), and $t_{1t,2t,3t}$ indicates the end of each unloading segment (S2).

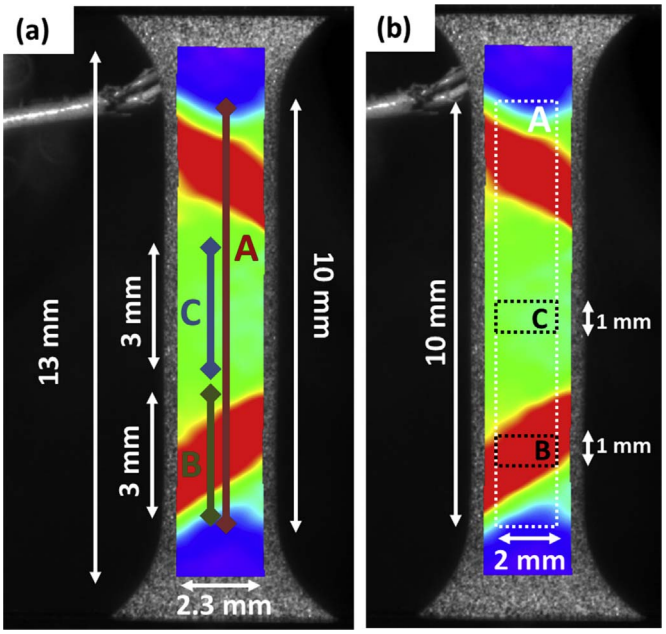

Fig. 3. Schematics to show the (a) digital extensometers and area of interest for DIC analysis, and (b) the areas where average strains are calculated.

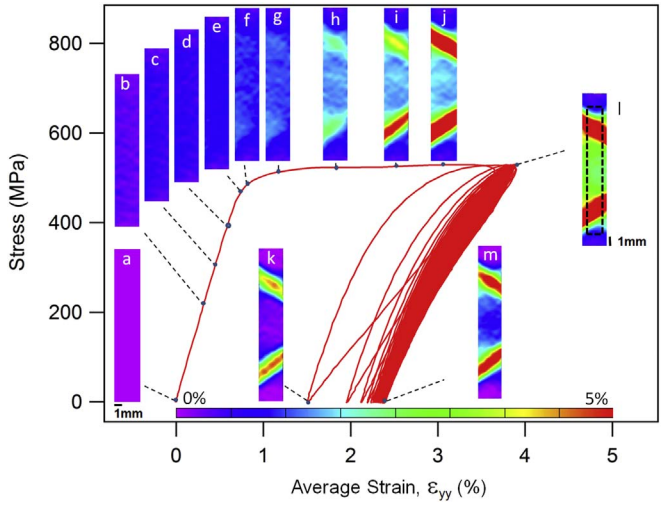

Fig. 4. Under force-control, the obtained stress-strain response for 100 cycles and associated strain contour maps.

3. Experimental observations

The experimental data analyses for both control modes are carried out systematically. In addition to the stress-strain curves, the applied force, displacement and average strains (the strain in the x-direction (e_{xx}), the axial strain (e_{yy}), and the surface shear strain (e_{xy})) are also plotted with respect to the time history in the following subsections.

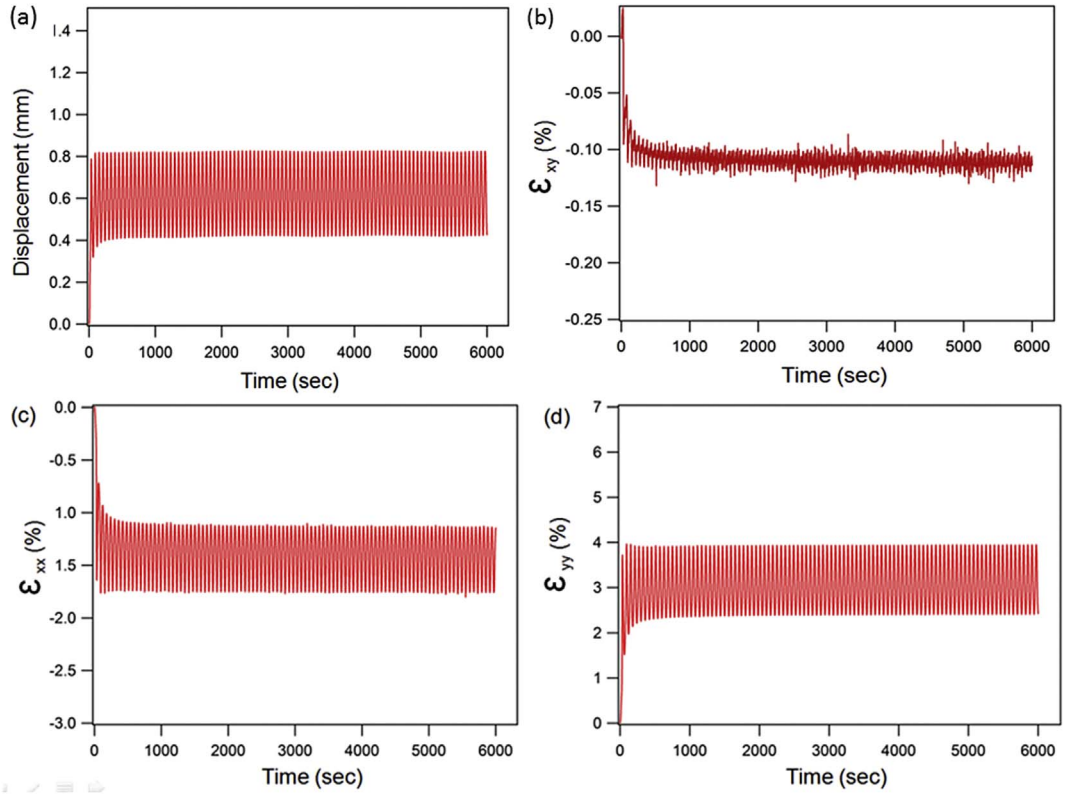

Fig. 5. Displacement, and average strains (e_{xy}, e_{xx}, e_{yy}) vs sinusoidal time history plots for force-controlled cyclic loading (100 cycles).

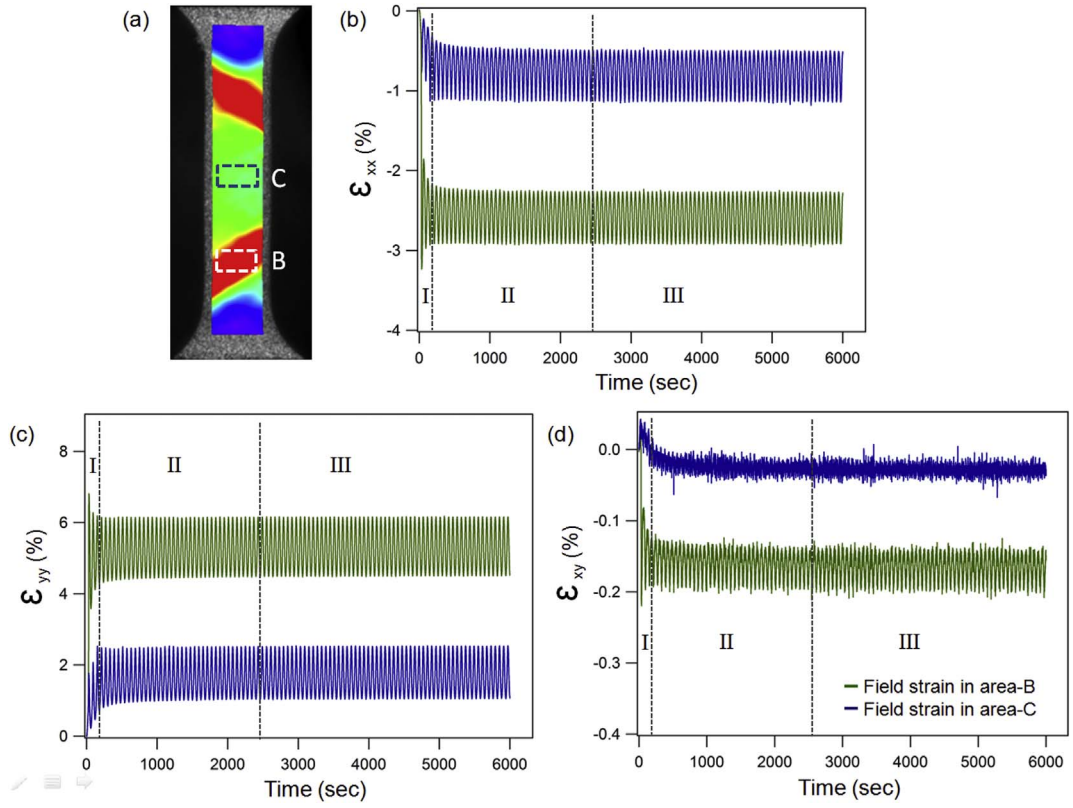

Fig. 6. Local field strains (e_{xx}, e_{yy}, e_{xy}) in the section-B and −C versus sinusoidal time history plots for force-controlled cyclic loading (100 cycles).

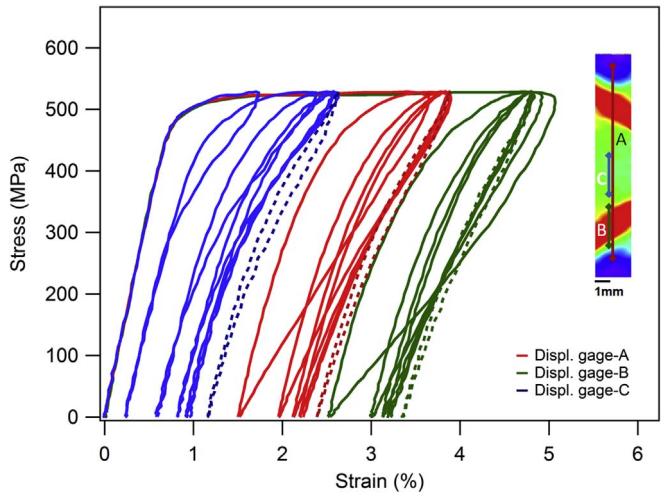

Fig. 7. Stress-strain response obtained from three different displacement gages (A, B, and C) for the first five cycles (solid lines) and the last cycle (cycle 100, dotted lines) under force-control.

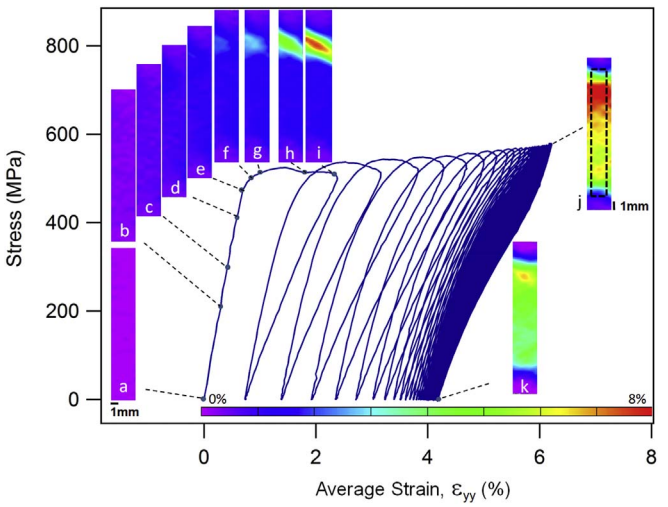

Fig. 9. Under mixed-control, the obtained stress-strain response for 100 cycles and associated strain contour maps.

Furthermore, the residual strain and the stress-strain hysteresis area are also plotted with respect to the increasing number of cycles in order to compare results covering both control modes.

3.1. Force-controlled (S1-force, S2 -force control) cyclic test results

The axial average strain, measured using the DIC digital extensometer which spans the specimen gage length, is plotted against the nominal engineering stress for 100 cycles in Fig. 4. During the loading of the first cycle a slightly increasing stress plateau is evident starting from 1.1% strain. A stress magnitude of 528.6 MPa is reached at the point "j" (in Fig. 4) with 2.91% strain. Subsequent cycles reach the same fixed stress magnitude. The unloading curve of the first cycle ends with 1.5% residual strain. For a detailed quantitative observation, residual strain, and stress-strain hysteresis area are plotted as a function of number of cycles.

The evolution of the displacement and average strains (e_{xx}, e_{yy}, e_{xy}) versus sinusoidal time histories are plotted in Fig. 5(a–d). These plots clarify effective parameters in force-controlled cyclic loading. In each figure, the total time history is 6000 s for 100 cycles. The applied force oscillates between 0 and 1648.5 N during cyclic deformation. The obtained total displacement is 0.78 mm in the first cycle. After 6 cycles, the minimum displacement becomes constant at 0.41 mm and remains constant until 100 cycles (see Fig. 5(b)). The transverse strain (e_{xx}), the axial strain (e_{yy}), and the surface shear strain (e_{xy}) averaged over the gage section (2 mm × 10 mm, illustrated in DIC image "l" in Fig. 4) are measured using DIC and plotted against time history in Fig. 5(b–d). With reference to Figs. 7 and 8, the strain measured in each direction approaches the stable stage after the early evolutionary stage (stage-I) and transient stage (stage-II). At the stable stage (stage-III), the measured maximum tensile strain in the axial direction was 3.92% while the corresponding compression strain in the x-direction and the surface shear strains were −0.71% and −0.12%, respectively.

To gain further insights into the stress-strain behavior, the relevant meso-scale DIC strain contours for the first and 100th cycles are added in Fig. 4. Only selected associated strain contour maps are shown in Fig. 4. The strains in these contours are the axial component of strain coinciding with the loading direction. The dashed boundary, within the image "l" delineates the region used to calculate the meso-scale field strain, as explained in Section 2. Note that a homogenous strain distribution is traced from the DIC images (image "a" to "e" in Fig. 4) until the stress magnitude of 480.9 MPa. After DIC image "f", the local strain heterogeneity initiates with further deformation during loading. The increase of the strain magnitude during loading is accompanied by the formation of local strain bands which are oriented at +61° and −62° from the loading axis as shown in Fig. 4. Note that the magnitude of the local strain the first cycle reaches 5% (image "j") while the maximum average strain is still 3.4% throughout the gage. At the end of the unloading, the severe strain localization has decreased (image "k") relative to its loading counterpart. After 100 cycles, more severe localized strain is observed (images "l" and "m") compared to their counterparts in the first cycle (images "j" and "k").

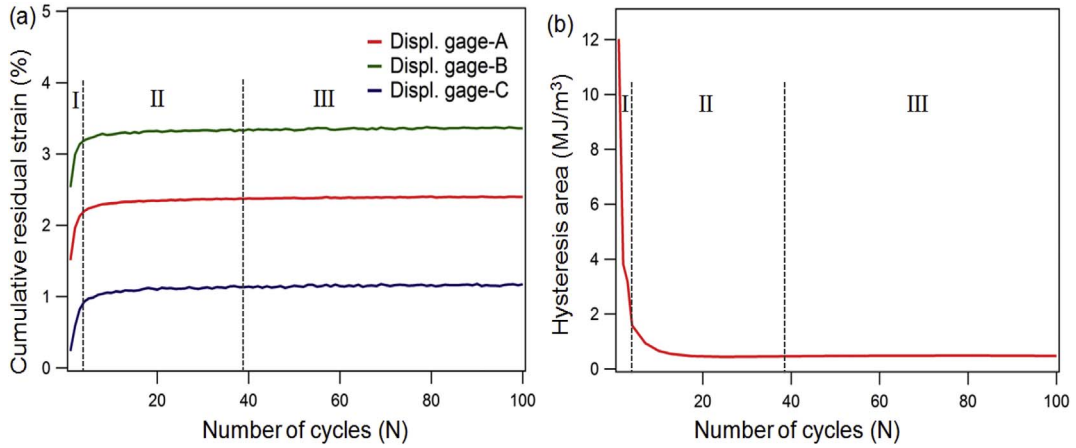

Fig. 8. Effective parameters in cyclic stress-strain response with respect to the cyclic number of cycles under force control: a) Cumulative residual strain (%), b) Hysteresis area (MJ/m^3).

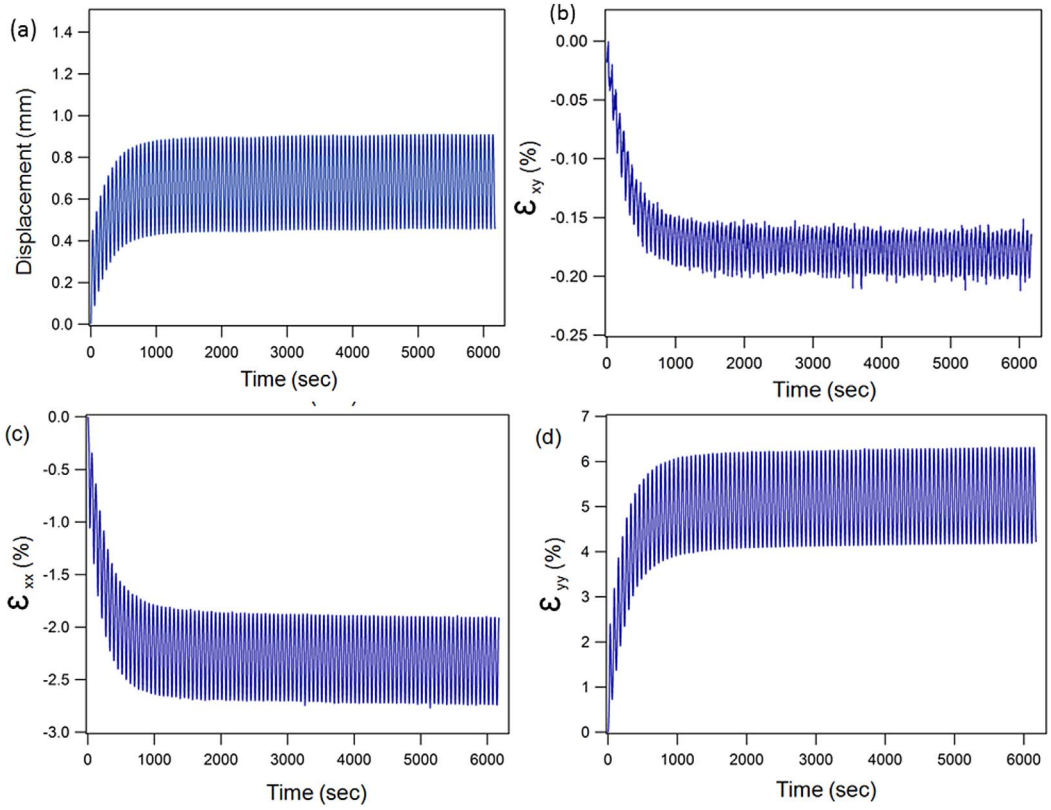

Fig. 10. Force, displacement, and average strain components (e_{xy}, e_{xx}, e_{yy}) vs sinusoidal time history plots for mixed-controlled cyclic loading (100 cycles).

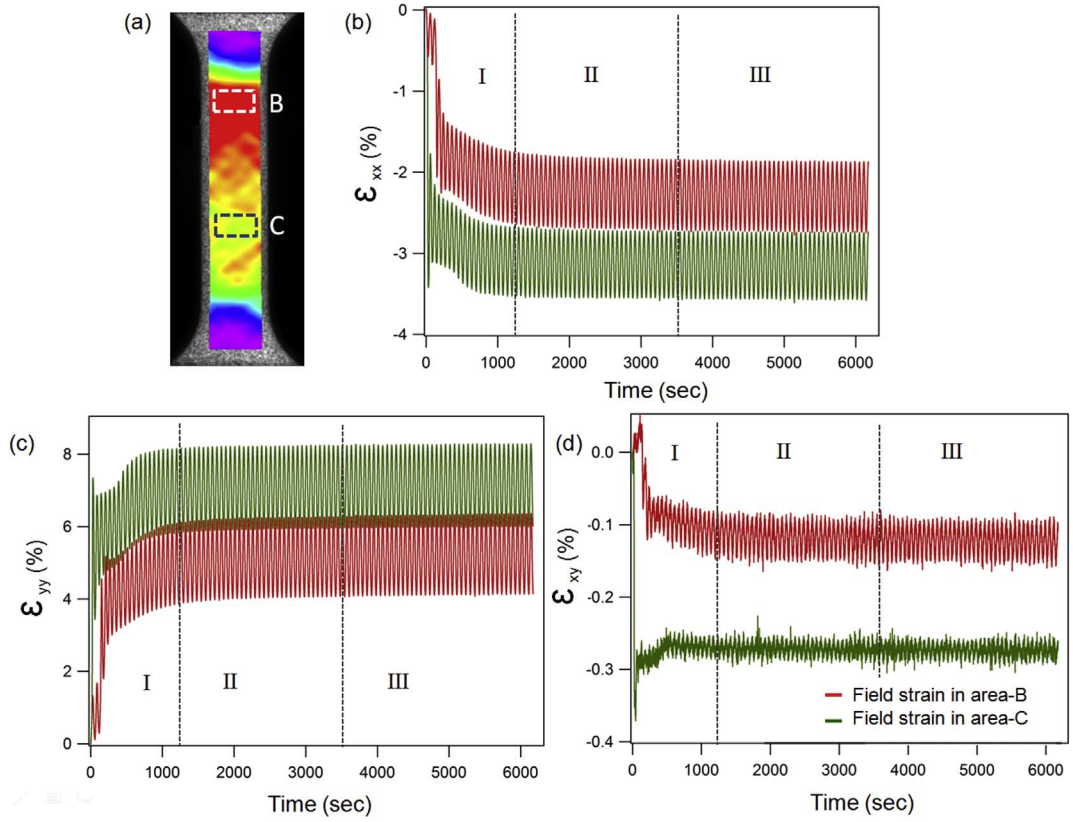

Fig. 11. Local field strains (e_{xx}, e_{yy}, e_{xy}) in the section-B and -C versus sinusoidal time history plots for mixed-controlled cyclic loading (100 cycles).

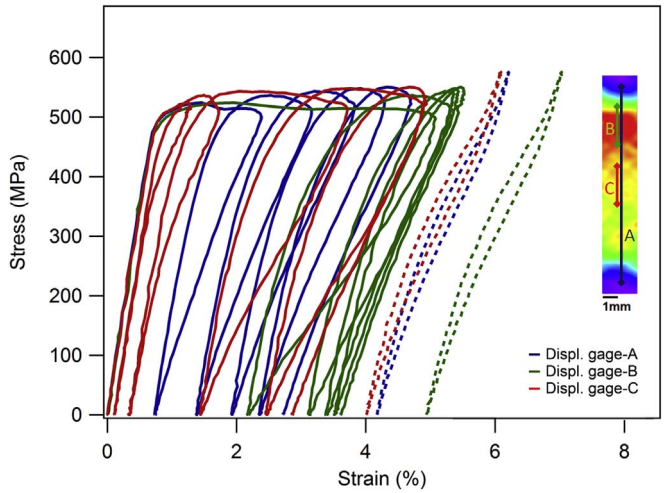

Fig. 12. Stress-strain response obtained from three different displacement gages (A, B, and C) for the first five cycles (solid lines) and the last cycle (cycle 100, dotted lines) under mixed-control.

In addition to the measured full field average strain on the digital extensometers, the local field average strains, which are measured inside and outside of the strain band (area-B and −C (2 mm × 1 mm) in Fig. 6 (a)), are also plotted against the time history. As can be seen in Fig. 6(b–d)), the local field average strains in the area-B and −C follow a similar evolutionary pattern though the strain values differ. In particular, the magnitude of the maximum axial field strain (e_{yy}) inside of the strain band stabilizes after 2340 s; it becomes 6.14% while the maximum axial field strain (e_{yy}) outside of the strain band is 2.5%. The stabilized strain inside of the strain band in the x-direction (e_{xx}) and the surface shear strain (e_{xy}) are −2.9% and −0.19% while their counterparts measured from the outside of the stain band are −1.12% and −0.04%, respectively.

To examine the local strain evolution, two different two-point DIC (digital extensometer) are located inside of the localized strain band (digital extensometer-B) and outside of the localized strain band (digital extensometer-C) as shown in Fig. 7. In addition to the average strain (digital extensometer-A), local strain at B and C are also plotted against the nominal stress for the first 5 cycles and the last cycle (cycle 100). The same initial linear elastic curve is obtained up to 150 MPa from three different digital extensometers during loading of the first cycle. However, the path of the non-linear deformation and the obtained final stress-strain loop (cycle 100, dashed line) varies for each digital extensometer as shown in Fig. 7.

The residual strain evolution throughout the digital extensometer-A for 100 cycles is plotted as a function of number of cycles in Fig. 8(a). It starts with 1.5% strain and shows an early evolution (stage-I) between cycles 1 and 3 and transient stage (stage-II) between cycles 3 and 39. The subsequent cycles after cycle 39 demonstrate a stabilized trend (stage-III) with 2.39% strain until 100th cycle. The residual local strain evolutions at two different regions (digital extensometer-B and −C in Fig. 7) are also plotted with respect to the number of cycles in Fig. 8(a). Similar stabilization patterns were observed for both gages throughout the 100 cycles. The stress-strain hysteresis area for each cycle was calculated and plotted as a function of number of cycles in Fig. 8(b). To calculate the stress-strain hysteresis area, the fifth order integral equations of the non-linear response was obtained using the curve fitting technique. The obtained cyclic evolutionary behavior of the hysteresis area consists of an early evolution (stage-I) until cycles 3, a transient stage (stage-II) between cycles 3 and 39, and nearly stabilized stage (0.47 MJ/m^3, stage-III) between cycles 39 and 100.

3.2. Mixed-controlled (S1-displacement, S2-force control) cyclic test results

The stress versus axial average strain response is presented in Fig. 9. During the first loading under displacement control, a stress-drop, 12 MPa, is observed during the non-linear deformation under displacement control. A similar response is observed in the non-linear part of the loading curves until cycle 17. Unloading starts under force-control mode after the point “i” and ends with 0.75% residual strain. To determine strain localization in the first and last cycles, the meso-scale in-situ DIC strain contours are also added on the stress-strain plot. As can be seen in Fig. 9, the initiation (see DIC image “f”) and propagation (see DIC images “g” - “i”) of the local strain band begins at 490.3 MPa in the first cycle. The observed localized strain becomes bigger in the 100th cycle (see DIC image “j”) compared to its counterpart in the first cycle (DIC image “i”).

The evolution of the applied sinusoidal force, displacement and average strains (ε_{xx}, ε_{yy}, ε_{xy}) versus time histories (6174.5 s) are plotted for the mixed-controlled cyclic test in Fig. 10(a–e). The magnitude of the maximum force reached in first cycle is 1600 N in the first cycle. The maximum force increases to 1660 N within 6 cycles as seen in Fig. 10(a). After the 6th cycle, the force remains constant until cycle 100. The initial change in displacement in the first cycle is 0.45 mm and becomes constant after 8 cycles (Fig. 10(b).). The strain in the x-direction (e_{xx}), the axial strain (e_{yy}), and the surface shear strain (e_{xy}) averaged over the gage section (dashed area (2 mm × 10 mm) in Fig. 9 image “j”) were measured using DIC and plotted against time

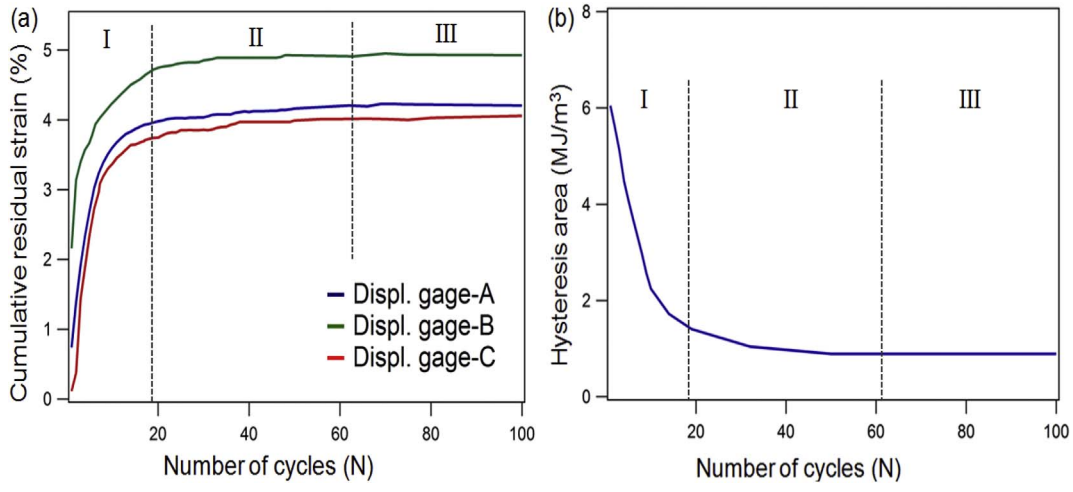

Fig. 13. Effective parameters in cyclic stress-strain response with respect to the cyclic number of cycles under mixed-control: a) Cumulative residual strain (%), b) Hysteresis area (MJ/m^3).

history in Fig. 10(b–d). After the early evolutionary and transient stages, all measures of strain approach the stabilization stage. At the stabilization stage, the measured maximum tensile strain in the axial direction is 6.2% while the corresponding compressive strain in the x-direction and the surface shear strains are −2.67% and −0.19%, respectively.

In addition to the average strain, the local field strains obtained from inside and outside of the strain band (area-B and −C (2 mm × 1 mm) in Fig. 11(a)) are also plotted against the time history. As can be seen in Fig. 11(b–d), the measured strains (e_{xx}, e_{yy}, e_{xy}) follow similar evolutionary pattern displaying an early evolution, transient and stabilization stages with increasing number of cycle. In particular, the magnitude of the maximum axial field strain (e_{yy}) inside of the strain band becomes 8.22% after 61 cycles while the maximum axial field strain (e_{yy}) outside of the strain band is 6.25%. The stabilized strain inside of the strain band in the x-direction (e_{xx}) and the surface shear strain (e_{xy}) are −3.54% and −0.29% while their counterparts measured from the outside of the stain band are −2.68% and −0.14%, respectively.

The strain evolutions within the localized strain band (digital extensometer-B in Fig. 12) and outside of the localized strain band (digital extensometer-C) are also plotted in Fig. 12 for the first 5 cycles and the last cycle (cycle 100) to reveal their particular stress-strain pattern. We observed that strain evolution in each digital extensometer initiated showing the same linear elastic slope but deviated during the non-linear response as can be seen in Fig. 12. Fig. 13 shows the residual strain and stress-strain hysteresis area versus number of cycles for the mixed-controlled test. Fig. 13(a) shows residual strain evolution throughout the gage for 100 cycles. The first cycle terminates with 0.75% residual strain. We note that the residual strain results are affected by the use of relative displacement control. After the first cycle, the observed evolutionary behavior of the residual strain consists of an early evolution (stage-I) between cycles 1 and 19, a transient stage (stage-II) between cycles 19 and 61 and a nearly stable stage (stage-III) between cycles 61 and 100 with 4.13% residual strain. In addition to the residual strain evolution throughout the gage, residual strain evolution at the digital extensometer-B and −C are also plotted in Fig. 13(a). Similar strain evolution patterns are obtained from both gages throughout the 100 cycles. Fig. 13(b) shows the stress-strain hysteresis area versus cycle number. The calculated hysteresis area for the first cycle, 6.05 MJ/m^3, decreases to 1.4 within 19 cycles during the early evolution (stage-I). A transient stage (stage-II) is observed between cycles 19 and 61. After cycle 61, it shows a nearly stable trend (~0.89 MJ/m^3, stage-III) until cycle 100.

4. Discussion

The mechanical responses under force and mixed controlled protocols are determined to compare their cyclic stabilization during 100 cycles at the macro-scale level. The plotted stress-strain responses (Figs. 4 and 9) show that a marked early stabilization occurs within the few cycles under force control compared to the mixed controlled counterpart. We note that relatively small residual strain is obtained under force-control. The force-controlled cycling contributes an early approach to saturation with lower residual strain compared to the mixed controlled counterpart under an equal number of load/unload cycles.

At the meso-scale level, in-situ experiments which are performed using DIC provide a unique opportunity to monitor and analyze the full-field average strains (the transverse, axial and surface shear strains) evolution under each control protocol during mechanical cycling. A homogeneous strain evolution which is obtained during initial loading stage is followed by a dynamic formation and gradual growth of localized strain bands for both cyclic experiments. However, smaller global deformation and narrow strain band are obtained from the pure force controlled cyclic test. In previous study, similar local strain bands are observed in the pure force controlled test by Zheng et al. [19]. In the literature, the observed strain heterogeneity has been attributed to the onset of austenite to detwinned martensite phase transformation [25]. We make the important observation that severe strain localization occurs under force control compared to the mixed controlled cyclic result. This stain localization shows a Luders-like deformation as typically observed for stress-induced martensite transformations [26]. We note that each control protocol creates different Luders-like deformation during mechanical cyclic stabilization. Moreover, the locally placed digital extensometer provided the data on the residual strain and stress-strain hysteresis area corresponding to the force and mixed controlled cyclic tests (Figs. 8 and 13). The residual strain is the irrecoverable deformation after a load-unload. During the pseudoelastic deformation in the austenitic phase, a partial phase transformation occurs from austenite to detwinned martensite. Upon unloading the partial reverse phase transformation occurs from detwinned martensite to austenite with the residual strain.

At the micro-scale level, the locally resolved strains data are extracted from both experimental results with detailed DIC in Figs. 6 and 11. The local field strains which are measured inside and outside of the strain band show an evolutionary response under both control modes. Particularly, the detected early evolution and transient stage under force control takes place within a lower number of cycles than the mixed-controlled counterpart for the transverse strain (e_{xx}), the axial strain (e_{yy}), and the surface shear strain (e_{xy}). Moreover, the obtained evolutionary behavior which consists of the early evolution (stage-I), transient stage (stage-II) and the following stabilization (stage-III), are distinctly different for both control modes. We note that the local field average strains follow a similar evolutionary pattern with the macroscopic counterparts throughout the 100 cycles. Additionally, linking the macro-scale response to the micro-scale local strain data, the employed loading mode dictates its own characteristics through the cyclic stabilization.

We finally note that the mechanical cycling of a NiTi SMA may be influenced by a combined effect of material and experimental parameters. The loading mode is one of the effective experimental parameters. It is clear from the experimental results that the selected loading mode in the experiment plays a significant role in dictating: (a) the evolutionary pattern of the stress-strain curves (b) the amount of cumulative residual strain, (c) the required number of cycles to approach to stabilization, and (d) the detailed shape of stabilized stress-strain hysteresis area. Considering cyclic stabilization state, it is desirable to reach a quick stabilization by the end of the initial cyclic protocol. Hence, the applied protocol for the stabilization of the NiTi SMA must be carefully selected with appropriate control mode before its service use in any stabilization required application.

5. Conclusions

The effect of the employed loading mode on the mechanical cyclic stabilization is investigated using uniaxial cyclic test for 100 cycles. The force-controlled cyclic test results were carefully compared with the mixed-controlled (S1-displacement, S2-force) counterpart at the macro, meso and micro-scale levels. At the macro-scale level, a significant reduction in number of cycles is detected under force control compared to the mixed control to obtain an early stabilization. The stress-strain curves created an evolutionary pattern consisting of three regions of stability which are an early evolution, transient stage and a nearly stable stage with increasing number of cycle. Similar evolutionary pattern were drawn from the plotted residual strain and the stress-strain hysteresis area. At meso and micro-scales, the detailed DIC analysis unveiled that severe strain localization is formed under force-controlled cyclic loading. Furthermore, the locally resolved strain data uncovered that the extracted evolutionally pattern is similar to the macro-scale observation for both loading modes. In the following study, the effect of the displacement control mode on the mechanical cyclic stabilization of the NiTi SMA will be examined.

References

[1] J. McCormick, D. Fugazza, F. Auricchio, R. DesRoches, Seismic vibration control using superelastic shape memory alloys, J. Eng. Mater. Tech. 128 (2006) 294–301.

[2] J.M. Young, K.J. Van Vliet, Predicting in vivo failure of pseudoelastic NiTi devices under low cycle, high amplitude fatigue, J. Biomed. Mater. Res. Part B-Applied Biomater. 72B (2005) 17–26.

[3] J.P. Oliveira, R.M. Miranda, N. Schell, F.M. Braz Fernandes, High strain and long duration cycling behavior of laser welded NiTi sheets, Int. J. Fatigue 83 (2016) 195–200.

[4] C. Morin, Z. Moumni, W. Zaki, Thermomechanical coupling in shape memory alloys under cyclic loadings: experimental analysis and constitutive modeling, Int. J. Plasticity 27 (2011) 1959–1980.

[5] B. Strnadel, S. Ohashi, H. Ohtsuka, S. Miyazaki, T. Ishihara, Effect of mechanical cycling on the pseudoelasticity characteristics of Ti-Ni and Ti-Ni-Cu alloys, Mat Sci. Eng. A203 (1995) 187–196.

[6] P.G. McCormick, Y. Liu, Thermodynamic analysis of the martensitic transformation in NiTi-II, Effect of transformation cycling, Acta Metall. Mater. 42 (1994) 2407–2413.

[7] M.A. Iadicola, J.A. Shaw, Effect of uniaxial cyclic deformation on the evolution of phase transformation fronts in pseudoelastic NiTi Wire, J. Intelligent Mater. Syst. Struct. 13 (2002) 143–155.

[8] R. DesRoches, J. McCormick, M. Delemont, Cyclic properties of superelastic shape memory alloy wires and bars, J. Struct. Eng. ASCE 130 (2004) 38–46.

[9] G. Kang, Q. Kan, L. Qian, Y. Liu, Ratchetting deformation of superelastic and shape-memory NiTi alloys, Mech. Mater. 41 (2009) 139–153.

[10] K. Gall, J. Tyber, G. Wilkesanders, S.W. Robertson, R.O. Ritchie, H.J. Maier, Effect of microstructure on the fatigue of hot-rolled and cold-drawn NiTi shape memory alloys, Mater. Sci. Eng. A 486 (2008) 389–403.

[11] A. Yawny, J. Olbricht, M. Sade, G. Eggeler, Pseudoelastic cycling and ageing effects at ambient temperature in nanocrystalline Ni-rich NiTi wire, Mater. Sc. Eng. A 481–482 (2008) 86–90.

[12] H. Sehitoglu, J. Jun, X. Zhang, I. Karaman, Y. Chumlyakov, H.J. Maier, K. Gall, Shape memory and pseudoelastic behavior of 51.5%Ni-Ti single crystals in solutionized and overaged state, Acta Mater. 49 (2001) 3609–3620.

[13] X. Liu, Y. Wang, D. Yang, M. Qi, The effect of ageing treatment on shape-setting and superelasticity of a nitinol stent, Mater. Charact. 59 (2008) 402–406.

[14] K. Gall, H.J. Maier, Cyclic deformation mechanisms in precipitated NiTi shape memory alloys, Acta Mater. 50 (2002) 4643–4657.

[15] H. Sehitoglu, R. Anderson, I. Karaman, K. Gall, Y. Chumlyakov, Cyclic deformation behavior of single crystal NiTi, Mater. Sci. Eng. A 314 (2001) 67–74.

[16] S. Nemat-Nasser, W. Guo, Superelastic and cyclic response of NiTi SMA at various strain rates and temperatures, Mech. Mater. 38 (2006) 463–474.

[17] O. Ammar, N. Haddar, L. Dieng, Experimental investigation of the pseudoelastic behaviour of NiTi wires under strain- and stress-controlled cyclic tensile loadings, Intermetallics 8 (2017) 52–61.

[18] Y. Zhang, Y. You, Z. Moumni, G. Anlas, J. Zhu, Experimental and theoretical investigation of the frequency effect on low cycle fatigue of shape memory alloys, Int. J. Plast. 90 (2017) 1–30.

[19] R.M. Tabanli, N.K. Simha, B.T. Berg, Mean stress effects on fatigue of NiTi, Mater. Sci. Eng. A 273–275 (1999) 644–648.

[20] W.R. Corwin, S.T. Rosinski, E. Van Walle (Eds.), ASTM STP 1329-Small Specimen Test Techniques, 1998, p. 576.

[21] W.H. Peters, W.F. Ranson, Digital imaging techniques in experimental stress analysis, Opt. Eng. 21 (1982) 427–432.

[22] S. Dilibal, Investigation of nucleation and growth of detwinning mechanism in martensitic single crystal NiTi using digital image correlation, Metallogr. Microstruct. Anal. 2 (2013) 242–248.

[23] B. Reedlunn, S. Daly, L. Hector Jr., P. Zavattieri, J. Shaw, Tips and tricks for characterizing shape memory wire Part 5: full-field strain measurement by digital image correlation, Exp. Tech. 37 (2013) 62–78.

[24] S. Daly, D. Rittel, K. Bhattacharya, G. Ravichandran, Large deformation of Nitinol under shear dominant loading, Exp. Mech. 49 (2009) 225–233.

[25] P. Sittner, Y. Liu, V. Novak, On the origin of Luders-like deformation of NiTi shape memory alloys, J. Mech. Phys. Solids 53 (2005) 1719–1746.

[26] Y. Liu, Y. Liu, J.V. Humbeeck, Lüders-like deformation associated with martensite reorientation in NiTi, Scr. Mater. 39 (1998) 1047–1055.